ELSEVIER

Materials Science and Engineering A 419 (2006) 153–161

MATERIALS SCIENCE & ENGINEERING A

www.elsevier.com/locate/msea

Surface composite fabrication using Fe-based alloying powder through infiltration casting technique on copper substrate

Gui-Rong Yang [a,*], Wen-Ming Song [a], Jin-Jun Lu [b], Yuan Hao [a], Ya-Min Li [a], Ying Ma [a]

[a] *State Key Laboratory of New Nonferrous Metal Materials, School of Materials Science and Engineering, Lanzhou University of Technology, Lanzhou 730050, Gansu, China*

[b] *State Key Laboratory of Solid Lubrication, Lanzhou Institute of Chemical Physics, Chinese Academy of Sciences, Lanzhou 730000, Gansu, China*

Received in revised form 6 December 2005; accepted 6 December 2005

Abstract

A process of vacuum infiltration casting technique for production of surface composite on copper substrate is presented. The surface infiltrated layer was fabricated on the copper substrate using Fe-based powder as surface alloying particles. The microstructure and several properties of the infiltrated layer have been studied. With an appropriate choice of processing conditions, a compact infiltrated layer is achievable through the SEM observation. The adhesion strength was evaluated through three-point bending test and thermal cycles. The macro-hardness of the infiltrated layer is about HRC 55 and the distribution of micro-hardness presents gradient change. The average micro-hardness of layer is about HV500. The thermal fatigue properties and oxidation resistance of infiltrated layer were tested at 800 °C. The number of thermal cycles reaches to 110 and 85 for infiltrated layer with a thickness of 1.5 and 2.6 mm, respectively. The infiltrated layer oxidized more rapidly than the substrate.

Keywords: Vacuum infiltration casting; Copper substrate; Microstructure; Properties of infiltrated layer

1. Introduction

High electrical and heat conductive copper is widely used in electronics and machinery, where higher strength and hardness are required. The failure of parts was always caused by the failure of the parts' surface. In order to improve surface properties of copper parts, a number of methods have been developed to improve the surface properties of copper including internal oxidation [1], chemical vapor deposition [2,3], electroplating [4], spray techniques [5], infiltration technique [6] and other means [7,8]. Of these methods, infiltration technique has the advantages of simplicity and feasibility over others in changing the characteristic of copper surface. Infiltration of a liquid metal into a preform can be carried out by pressureless or pressure-assisted methods. The main advantages of pressure-assisted infiltration include the following: (a) faster process; (b) near-net shape processing; (c) reduced contamination; (d) reduced porosity in comparison with spray techniques [9–20]. However, even in the case of pressure-assisted infiltration, choking of pores during infiltration can occur, which prematurely terminates the infiltration process [13]. This difficulty of achieving full infiltration increases with decreasing particle size in the preform and pouring temperature.

In this study, the bronze matrix surface composites were fabricated by the vacuum infiltration casting technique. The present article deals with the performance evaluation of some infiltrated layer in terms of hardness, adhesion (bond) strength, thermal fatigue and oxidation resistance.

2. Experimental procedures

2.1. Fabrication of infiltrated layer

In this work, Fe-based alloying particles, whose main ingredient are 30 wt.% Cr, 4 wt.% C, 5 wt.% Ni, 2.5 wt.% Si, 2 wt.% B, Fe (wt.%, in Bal.), of 120–160 mesh was chosen as the reinforcement, which is a kind of self-fusion alloying powder. Basic structure of this powder is hypereutectic ledeburite. Bronze ZQAl 9-4, with its composition listed in Table 1, was chosen as the matrix of the surface composite layer and the substrate material on which the infiltrated layer is formed.

* Corresponding author. Tel.: +86 931 2973640; fax: +86 931 2755806.
E-mail address: yanggrming@lut.cn (G.-R. Yang).

0921-5093/$ – see front matter © 2005 Elsevier B.V. All rights reserved.
doi:10.1016/j.msea.2005.12.010

Table 1
The chemical composition of tested aluminum bronze (wt.%)

Cu	Al	Fe	Sb	Si	P	As	Sn	Pb	Mn	Zn	Total
Bal.	8.0–10.0	2.0–4.0	≤0.05	≤0.2	≤0.1	≤0.05	≤0.2	≤0.1	≤0.5	≤1.0	≤1.0

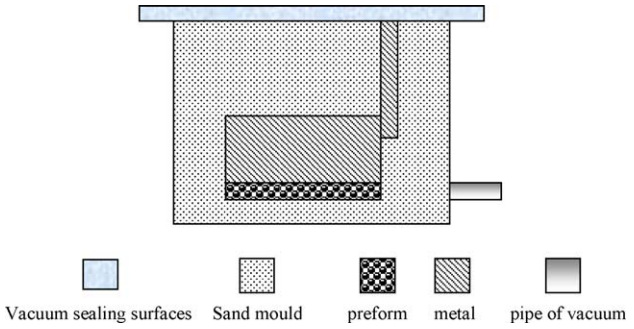

Fig. 1. The sketch of forming surface composite.

The surface infiltrated layer was fabricated by a vacuum infiltration casting process. Firstly, the Fe-based alloying powder and some self-fabricated bond NJB (its main composition is boric acid) were mixed together according to desired proportion, paved on inner surface of a casting mould or outer surface of mould cores, where the characteristic were needed to be improved. Then the mould or mould cores was heated to form solid preform layer at 150 °C under the condition of atmosphere. Secondly, the melt of bronze was poured into the mould at 1220 °C under vacuum. The mould was to be preheated to 150 ± 10 °C. By sucking force of the vacuum, the melt was infiltrated into the preform, and the surface composite layer was obtained after solidification of casting. The fabrication principle is shown in Fig. 1. The surface composites with differential thickness could be obtained through fabricating differential thickness of preform. The thickness of surface composite could reach 3.0 mm.

2.2. Microstructure and evaluation of properties

2.2.1. The microstructure of infiltrated layer

The microstructure of surface composite layer was observed by scanning electron microscope (SEM) of HITACHI S-520. The specimens for SEM observations were cut along the direction from composite surface to substrate, ground and polished using standard metallographic techniques.

2.2.2. Hardness and adhesion (bond) strength measurements

The macro-hardness has been measured using HRS-150 Rockwell hardness tester. The experimental load was 1471 N. The micro-hardness has been measured using HVS-1000 microhardness tester at load of 9.8 N and loading time of 20 s. A three-point bend test was employed to evaluate the adhesion (bond) strength. The dimensions of the specimens used in the bend tests were 5 mm × 5 mm ×40 mm and the thickness of surface infiltrated layer was 1.5–3.0 mm. Fig. 2 shows the design of the specimens used for the three-point bend tests. The infiltrated layer was located on the top (Fig. 2a) or at the bottom of the specimen. Load was applied to the specimen slowly with a definite displacement. After loading, the stress–strain curve was obtained. This curve was transformed to the load–displacement curve using a computer program. This test was conducted on three specimens for each type of bend test.

2.2.3. Thermal cycling experiment

The dimensions of the specimens used in the thermal cycling (thermal fatigue) experiment were 5 mm ×5 mm × 10 mm. For the thermal cycling, the specimens were heated in a muffle furnace and kept at 800 °C for 15 min, which was followed by water cooling. The temperature of cooling water is 20 °C. During cooling, the specimens were hold in a basin with cool water for 5 min. The specimens were taken out. Its temperature was same to that of water at that time, meanwhile, a thorough visual scrutiny of the specimens was undertaken to evaluate the extent of damage they have undergone within the substrate, at the interface between the bond and the surface layer, and on the top surface of the infiltrated layer. This thermal cycling was repeated many times.

2.2.4. Oxidation experiment

The oxidation behavior of the infiltrated layer was evaluated by the weight changes. Six surfaces of rectangular test specimens with dimensions 40 mm × 40 mm × 10 mm were ground, ultrasonically cleaned in water, and then rinsed in ethanol prior

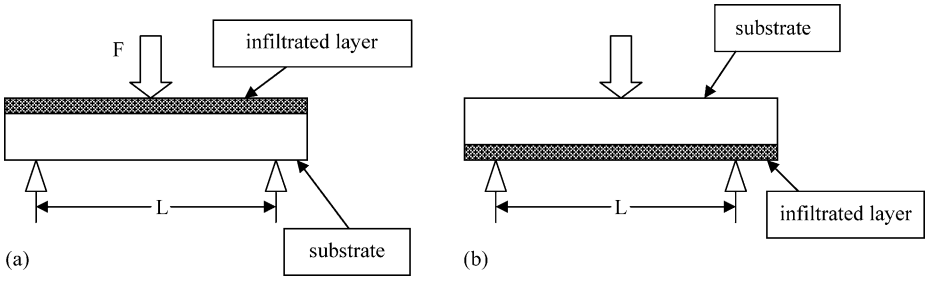

Fig. 2. The type of three-point bend test specimen for infiltrated layer. (a) Infiltrated layer on the top of the specimen and (b) infiltrated layer on the bottom of the specimen.

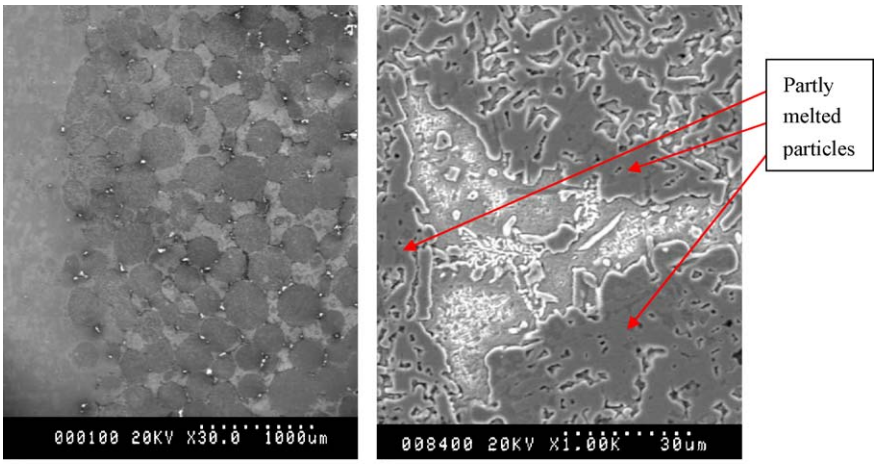

Fig. 3. The SEM of infiltrated layer.

to drying in air. The initial weight of specimens was measured using a photoelectric analytic balance with a precision of 0.1 mg. The specimens were heated in a muffle furnace kept at 800 °C for 2 h under the condition of atmosphere, and then cooled in atmosphere to room temperature, then weighed specimens. This test was repeated until the change of the specimen weight was near to zero. The time of heating specimen lasted for 4, 8, 12 and 24 h, respectively. Weight of the specimens was measured before and after each test to obtain the weight changes. Three specimens were performed in test to get the average oxidation rate.

3. Results and discussion

3.1. Microstructure of infiltrated layer

Cross-sectional view of the infiltrated layer is shown in Fig. 3. The micrographs reveal continuous and sound interfaces between the substrate and the infiltrated layer without any cracks. No spalling or separation is observed from the micro-cross-sectional view. The infiltrated surface composite layer doesn't show the obvious delamination structure. The Fe-based alloying particles within the infiltrated layer are distributed uniformly as shown in Fig. 3(a). Fig. 3(b) shows the interface between the partially melted Fe-based particles and the substrate.

The forming of infiltrated surface layer is fusion of Fe-based particles' surface with copper substrate. The melt point of Fe-based alloying powder is 1100 ± 50 °C, which is somewhat equivalent to the melt point of the matrix and its self-fusion effect is not very effective due to a low content of eutectic mixture with lower melting point in the Fe-based alloying powder. After pouring the melt, the melt infiltrated into the pores and permeated the preform. The temperature of molten copper alloy decreases somewhat owing to endothermic action of the mould. Hence, only the surface of the powder particles melts, decompose and diffuse within the interface between the substrate and particles. At the interfaces between the Fe-based particles and the melt, occurrence of metallurgical fusion gives birth to the formation of Cu-based solid solution and low melting eutectic phase. The eutectic phase of Al and Si separates from the liquid metal. Fig. 4 shows that Al and Si concentrate mainly in the area between the particles. In this area, Al in the eutectic phase comes from the matrix and Si comes from liquid metal of melted surface of the particles (Fig. 5). The volume fraction of eutectic Al–Si phase separating from the liquid metal is too small to be showed by a XRD pattern illustrated in Fig. 6. Around the grain exists Ni–Cr and Ni–Cr–Fe intermetallics that could be detached from Figs. 4 and 6.

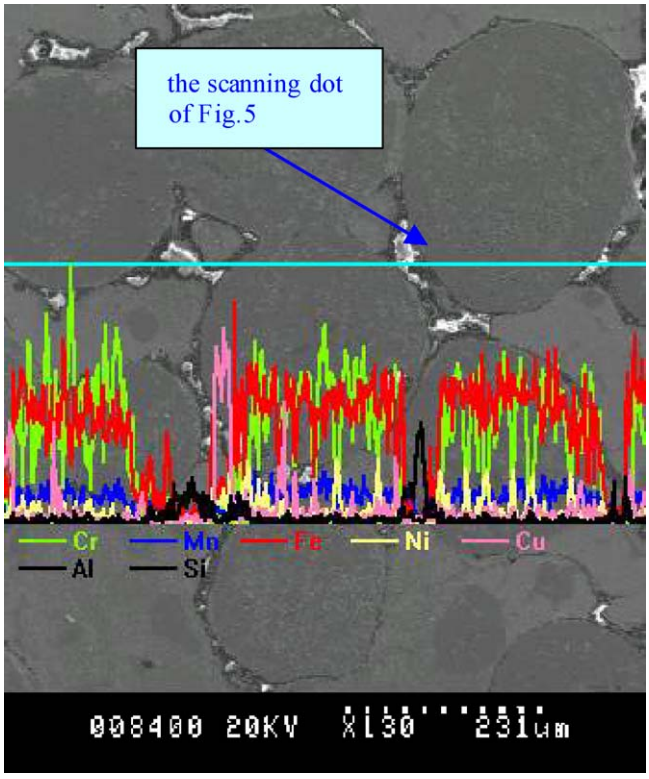

Fig. 4. Line scan of infiltrated layer.

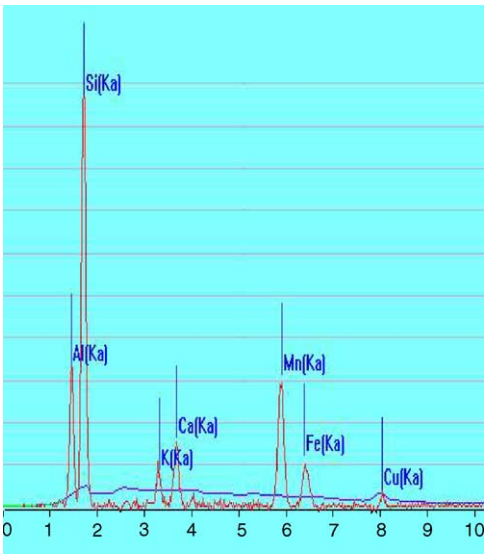

Fig. 5. EDS spectrum of infiltrated layer between the infiltrated grain.

3.2. Hardness and adhesion (bond) strength

3.2.1. The macro-hardness

The hardness of infiltrated layer is about HRC 55. While, the hardness of copper alloy is about HRB 130. The hardness of infiltrated layer has been improved largely. The reason of increasing hardness is the existing of boride, Ni–Cr and Ni–Cr–Fe intermetallics in the outer layer.

3.2.2. The micro-hardness

Fig. 7 shows the variation of average micro-hardness of infiltrated layer. The micro-hardness of outer layer is not the highest because the outer layer near the casting mould contains unavoidably shrinkage porosity because of the chilling action of preform and mould that leads to imperfect fusion. The micro-hardness reaches the largest value in the sub-surface layer because its quality of fusion is better than the outer layer. The structure of this layer is compact, and it contains some hard intermetallic phases. The composition of the un-melted particles is mainly hypereutectic ledeburite. The hardness of infiltrated layer drops sharply when the distance is near to 2.3 mm from the surface.

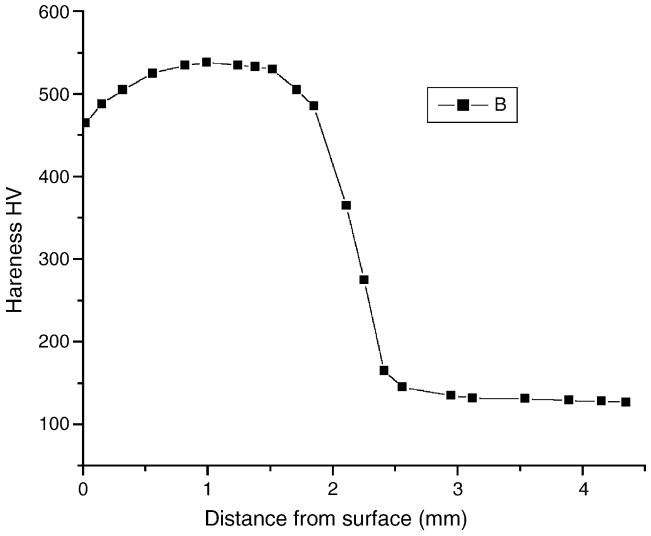

Fig. 7. The changing of average micro-hardness of infiltrated layer.

It can be explained by the fact the infiltrated layer is surface composite materials, in which the powder particles distributed uniformly and the diffusion only happened within about 200 μm. so there is no longer diffusion area (transition layer) between the substrate and the infiltrated layer (Fig. 4).

3.2.3. Adhesion strength

Fig. 8 shows the bending strength of specimen with infiltrated layer located at the bottom of the specimen. There is a small hackly change within the process of stress increasing comparing with that of the substrate (Fig. 9), and then the stress–strain changing is similar to that of the substrate as shown in Fig. 9. The yield strength (σ_p, 0.2) of the specimen with infiltrated layer is close to that of the substrate. In the course of test, we can hear the sound of cracking when the hackly curve appears, which suggest that the infiltrated layer has been destroyed. The main components of the infiltrated layer are hard and brittle phases such as the cementite and other intermetallics. Fig. 10 is the SEM after bending test. The substrate belongs to a ductile material and the surface layer is a brittle material from the analysis about the structure of infiltrated layer above mentioned, so the strain is different while the same stress. The infiltrated layer is at

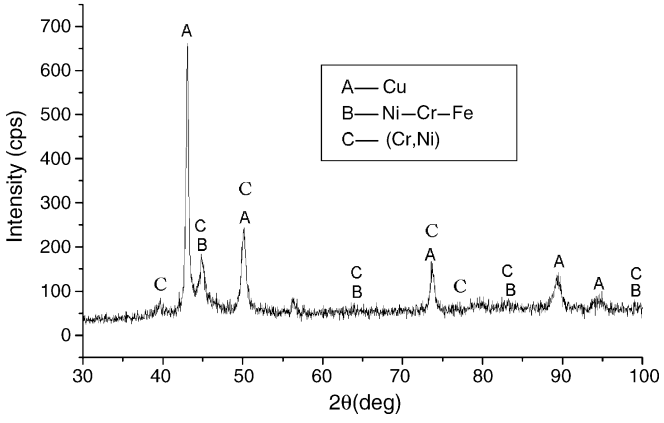

Fig. 6. XRD of infiltrated layer.

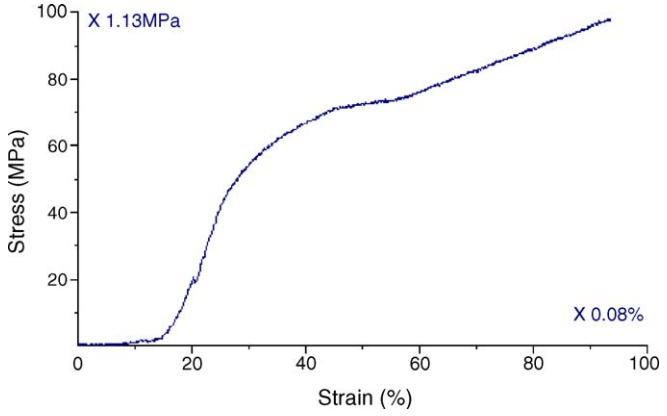

Fig. 8. The bending strength of specimen with infiltrated layer in the bottom.

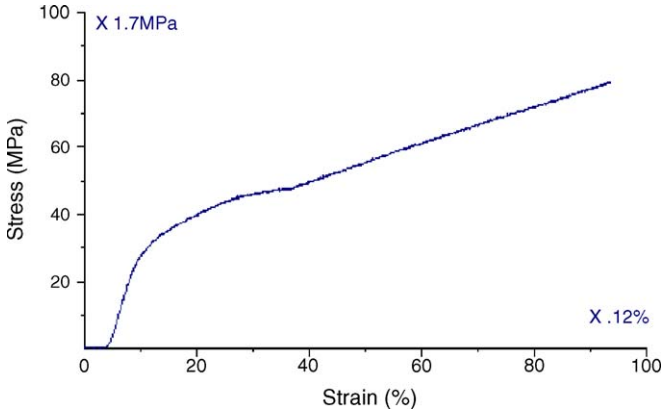

Fig. 9. Bending strength of the substrate.

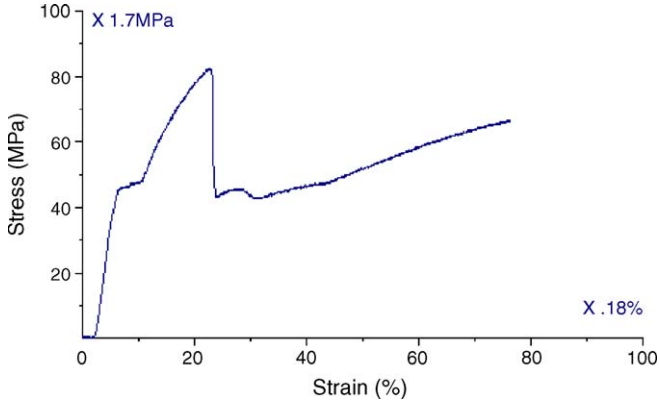

Fig. 11. The bending strength of specimen with infiltrated layer on the top.

the bottom of the specimen and its deformation and stress were larger than that of the substrate under the situation of this test. Therefore, stress between substrate and infiltrated layer happens. From the Fig. 10, we can see that a crack formed at the interface. The crack generated at the end of the vertical crack that is sensitive position of the crack. Then the crack grows along the interface with the increasing stress between the substrate and the infiltrated layer because of no transition layer between the substrate and the infiltrated layer.

The bending strength of the specimen with infiltrated layer located on the top of the specimen is shown in Fig. 11. We can see that the stress–strain curve is obviously different from that shown in Figs. 8 and 9. There is a yield point elongation, and then the stress increases with the increasing of the strain. After reaching a peak value, the stress drops rapidly. Then the stress–strain curve was similar to that of the substrate. The yielding strength of the specimen with infiltrated layer has been improved by 31% comparing to that of the substrate. The bending strength has been improved by 78% at the same strain of corresponding to a peak value comparing with the bending strength of the substrate. The infiltrated layer was located on the top of the specimen. At the beginning of the bending, the deformation of substrate is larger than that of the infiltrated layer and the strain is small at the beginning of the deformation, so the deformation of infiltrated layer can accommodate with the strain of substrate. The strength of infiltrated layer with hard particles is higher than that of the substrate. When the yield point elongation appears, the accommodation begins to decrease. The stress goes on increasing. Therefore, the yielding strength was improved and strengthening limit (the peak value) appeared. When the deformation was increased, the accommodation was destroyed. The stress between the infiltrated layer and the substrate appears on account of their different strain. The infiltrated layer was destroyed when the stress increased and exceeded the enduring limit.

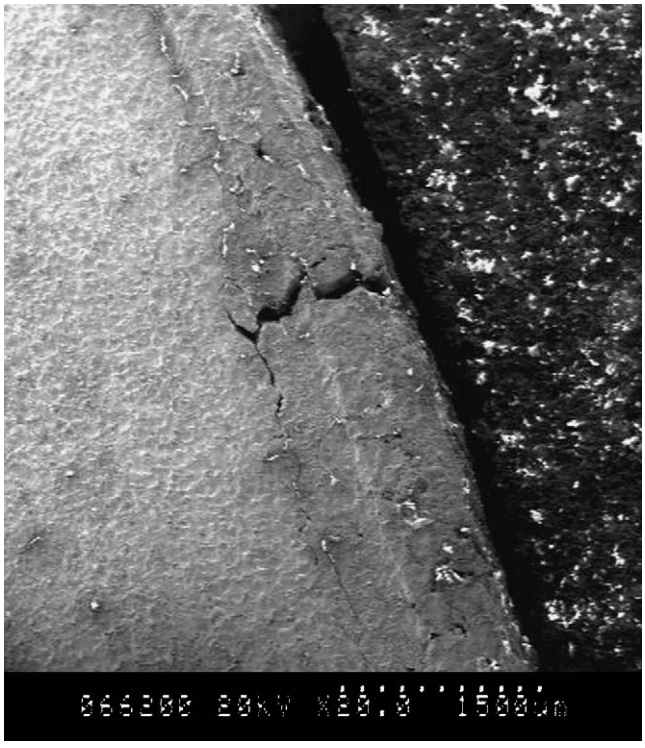

Fig. 10. Fracture SEM of the specimen with infiltrated layer at the bottom.

Fig. 12 shows the SEM micrograph of the fractured layer. The fracture SEM appearance of surface composite when the infiltrated layer located at bottom is same to that of being on the top. The particles are pulled out from the substrate because the strength of the particle is higher than that of substrate as shown in Fig. 13. From the appearance of substrate, the bending failure belongs to ductile fracture. While, from the fracture appearance of infiltrated layer, there are whole particles at the fracture appearance. It is different from classical ductile fracture. The bending failure of surface composite belongs to like-ductile fracture.

During the test, the bending strength of specimen changed little for differential thickness (1.5–3.0 mm) of surface infiltrated layer. Each specimen was subjected to visual evaluation after destroying. It was found that the destroying mode was similar for different situation of the infiltrated layer. The difference is that the strain was tensile stress when the infiltrated layer located at the bottom, and compress stress when infiltrated layer located on the top. Their destroying type was like-ductile fracture. The bending strength of specimen has been improved largely due to the existence of the infiltrated layer, especially for the layer on the top of specimen. The surface infiltrated layer belongs to com-

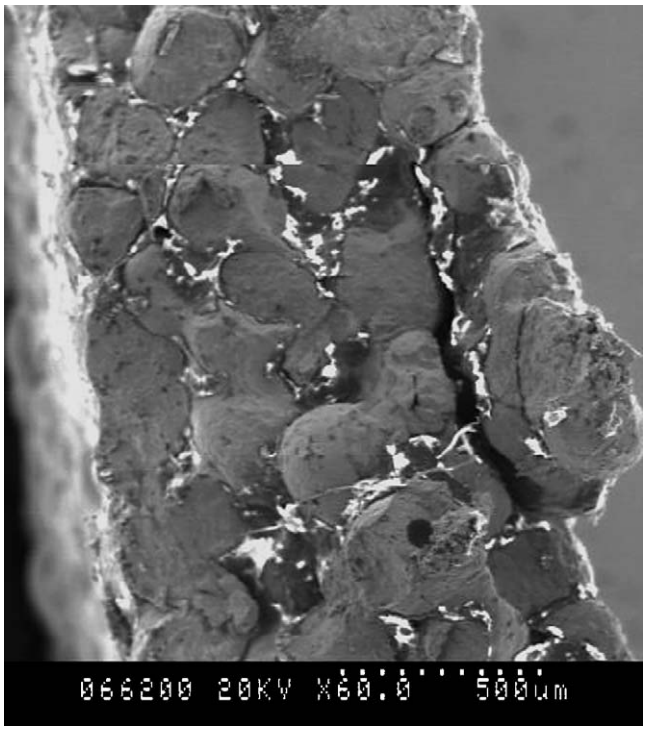

Fig. 12. Fracture appearance SEM of infiltrated layer.

posite with many particles reinforced, so its strength is higher than that of the substrate. The strength of surface composite could strengthen the strength of the whole specimen before the accommodation of strain between the surface infiltrated layer and substrate destroyed.

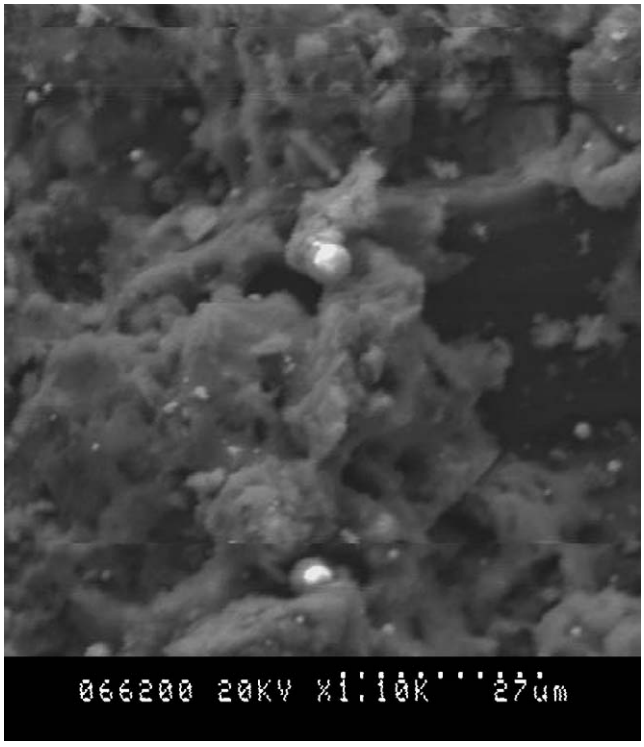

Fig. 13. The fracture appearance SEM of substrate.

Table 2
Results of the thermal cycling test

Thickness of infiltrated layer (mm)	Cycles conducted	Observations
1.5	110	Substrate and infiltrated layer oxidation were detected after the 20 times cycles; 1.5 mm infiltrated layer remains fine, micro-crack in the interface between the layer and substrate appear after the 78 times cycles; after the 91 times cycles, the surface of infiltrated layer appears the micro-crack; no obvious changes after 110 times cycles
2.6	85	Substrate and infiltrated layer oxidation were detected after the 20 times cycles; infiltrated layer remains fine, test is conducted after the 62 times cycles, cracks in the interface between the layer and substrate appear; after the 72 times cycles, infiltrated layer arched and the micro-crack appears on the surface of the infiltrated layer; after the 85 times cycles, the infiltrated layer spalls off from substrate

3.2.4. Thermal cycling

The performance of the infiltrated layer under thermal cycling conditions is mainly governed by the stresses developed at the infiltrated layer–substrate interface because of the difference in the thermal expansion coefficients [21]. The responses of the infiltrated layer to thermal cycling between 800 °C and cool water temperature are reported in Table 2. Fig. 14 is the scheme of the arched infiltrated layer after the 61 cycles. The dimensions of the specimen was 5.0 mm × 5.5 mm × 9.8 mm after the thermal experiment, while the dimensions of the specimens was 5.0 mm × 5.0 mm × 10 mm before thermal experiment. This was because the difference stress between the surface infiltrated layer and the substrate resulted in the differential distortion.

It is interesting to note that the infiltrated layer offers good thermal fatigue resistance. It is evident that the thermal fatigue resistance of thinner layer (1.5 mm) is better than that of thicker layer (2.6 mm). The main problem arises because of the oxidation of the infiltrated layer and substrate. A point to be considered is that these layers are subjected to very severe testing conditions corresponding to accelerated tests. However, these layers will not experience such severe conditions during applications. It may be noted that all tests have been concluded because of a significant oxidation of the infiltrated layer and the substrate. Figs. 15–17 was the SEM micrographs of the surface and the interface of infiltrated layer showing crack or spalling off. From Fig. 15, there was partly oxidation at the interface. The

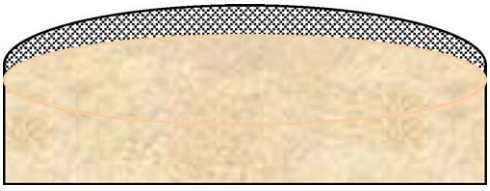

Fig. 14. The scheme of the arched infiltrated layer.

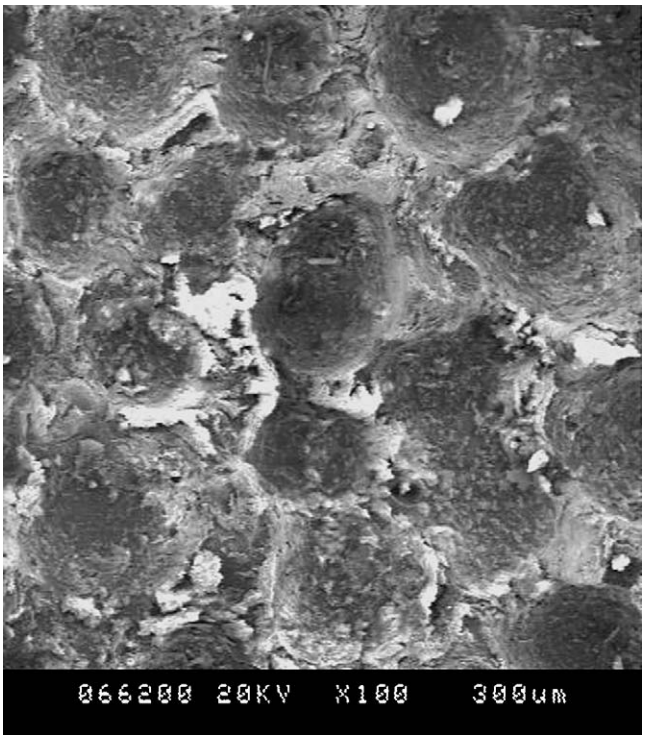

Fig. 15. The appearance of substrate after the infiltrated layer spalling.

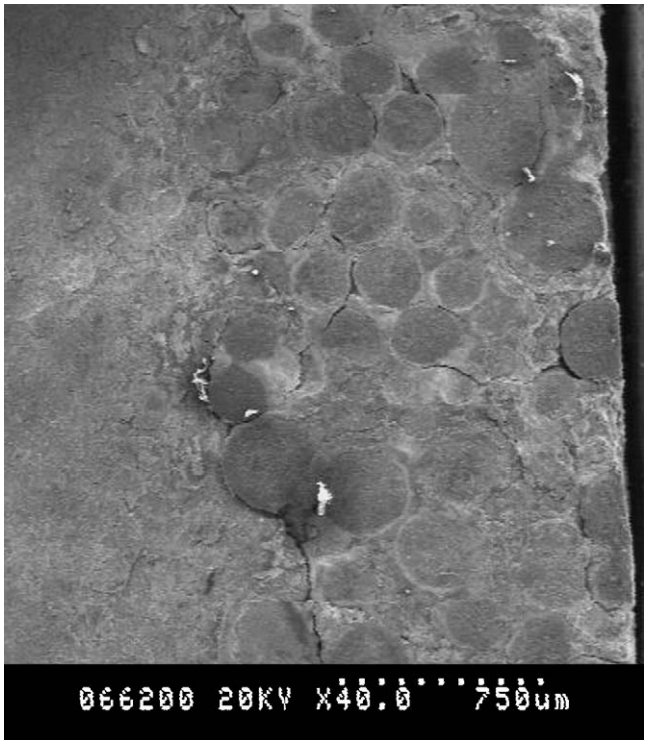

Fig. 17. The SEM of interface between infiltrated layer and substrate.

crack on the surface of infiltrated layer was around the particles. Fig. 16 shows that the micro-crack was mostly around the particles because of the differential thermal expansion coefficient between the particles and the matrix.

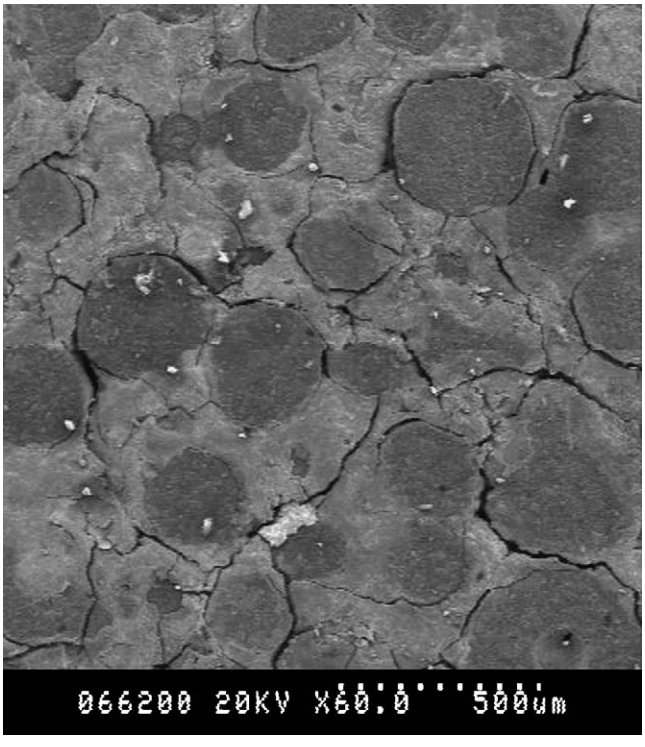

Fig. 16. The appearance of infiltrated layer.

The most outer surface of the infiltrated layer is not somewhat compact, which may accommodate the thermal expansion coefficient mismatch more effectively [21]. The main composition of Fe-based alloying powder is Fe, Cr, Ni, Si and B. Their mean thermal expansion coefficients are presented in Table 3. From Table 3, it appears that the thermal expansion coefficient of Ni is similar to that of the substrate Cu. But the main element of the alloying powder Fe-based alloying powder is Fe. The difference of thermal expansion coefficient of Fe and Cu is somewhat much more. The elements such as Cr, Ni, B and Si exist in state of intermetallic compounds. The stress between the particles and the substrate is much larger when cooling sharply. So the cracks generate easily around the particles in the most cases. The most cracks belong to vertical crack. Only one horizontal crack appears at the interface between the substrate and the infiltrated layer (Fig. 17). The stress concentration could be reduced happened at the interface between surface layer and substrate because the substrate is tough materials. The stress among the particles in the horizontal direction was not be reduced due to the content of copper was less than that of interface between surface layer and substrate.

Table 3
Mean thermal expansion coefficient, α ($^{\circ}C \times 10^{-6}$) [22]

Cu	17.0
Fe	11.76
Cr	6.2
B	8.3
Si	2.8–7.2
Ni	13.4

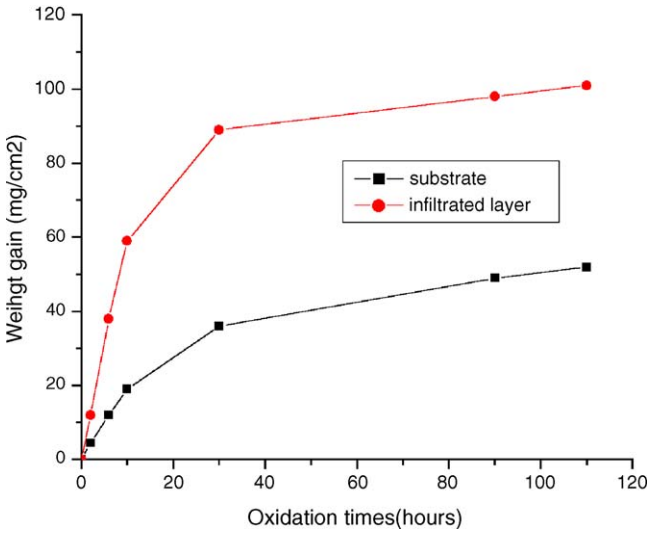

Fig. 18. Weight gain vs. oxidation time curves at 800 °C.

3.2.5. Oxidation

Fig. 18 shows the weight gain at 800 °C up to about 110 h for the substrate and infiltrated layer studied. It is apparent that the oxidation rate of infiltrated layer is higher than that of the substrate. The mass gain curves can be divided into two parts separated by a transition zone. The first stage, at very short oxidation times, is characterized by a rapid increase in the mass gain. For longer oxidation times, the oxidation behavior tends to constant.

The oxidation resistance of the alloys depends on their ability to form stable and slowly growing protective oxides, normally corresponding to Cr_2O_3, formed by selective oxidation of the corresponding alloy components [23,24]. For alloys containing chromium as a protective component, such as Fe-based alloy, the critical Cr content required to form exclusive external Cr_2O_3 scales is usually about 15–25 wt.% [24,25]. Although the Fe-based alloying powder used for fabricated infiltrated layer contain about 28 wt.% Cr, the oxidation resistance is improved to certain extent. The surface of the infiltrated layer is Fe–Cu alloy. The air oxidation of cast Fe–Cu alloys produce complex scales, usually containing mainly Fe_3O_4, Fe_2O_3, FeO and some small incontinuous outer layer of copper oxide ($CuO + Cu_2O$) plus an inner region composed of a mixture of the oxides of mainly two components as well as of some double Fe–Cu oxides [26,27]. The chemical activation of Fe is higher essentially than that of copper. There was no compact oxidation film produced during the oxidation test for protecting the inner part from keeping oxidation. The oxygen atom could penetrate through the loose oxidation surface into the inner, which result in the more oxidation. The infiltrated layer oxidizes generally more rapidly than the substrate. A possible reason for this effect is copper oxidizes more slowly than iron at 700 and 800 °C [26,27].

4. Conclusion

The results show that the infiltration casting process can be used for the fabrication of infiltrated layer with excellent properties. Fe-based powder has been successfully used as infiltration alloying powder to obtain good infiltrated layer on copper substrate. The infiltrated layer has clearly excellent interfacial boundaries, as apparent from their cross-sectional micrographs. The infiltrated layer had no lamination structure, so it belongs to surface composite material.

The macro-hardness of infiltrated hardness reaches about HRC 55, and highest micro-hardness is HV 530. So the hardness of infiltrated layer has been improved largely compared with the substrate. The tests of three-point bending and thermal cycling suggest good bonding between the infiltrated layer and the substrate. The bending strength has been enhanced to a certain extent. The difference of thermal coefficient of all kinds of elements is not much more, so the layer offers excellent thermal fatigue property. The oxidation resistance of the infiltrated layer was not good as well as the substrate.

Acknowledgements

The authors are pleased to acknowledge the financial support for this research provided by the National Natural Science Foundation of Gansu Project (ZS021–A25–024–C), the Chun-Hui Plan of Education Department of China project (Z2004-1-62013) and Young Teacher Startup Foundation project of Lanzhou University of Technology.

References

[1] S. Ziyuan, W. Deqing, J. Mater. Sci. Lett. 17 (6) (1998) 477–482.
[2] D.G. Bhat, H.E. Rebenne, C. Strandberg, J. Mater. Sci. 26 (7) (1991) 4567–4578.
[3] M.D. Feldslein, Plat. Surf. Finish. 85 (3) (1998) 248–255.
[4] D.D. Himbeault, R.A. Varin, K. Piekarski, Metall. Trans. A 19A (8) (1988) 2109–2123.
[5] S. Das, P.P. Bandyopadhyay, T.K. Bandyopadhyay, S. Ghosh, A.B. Chattopadhyay, Metall. Mater. Trans. A 34A (2003) 1909–1917.
[6] J. Lapin, D. Tiberghien, F. Delannay, Intermetallics 8 (2000) 1429–1438.
[7] S. Abraham, B.C. Pai, K.G. Satyanarayana, V.K. Vaidyan, J. Mater. Sci. 25 (8) (1990) 2839–2851.
[8] B. Kazimierzak, Mater. Des. 13 (2) (1992) 67–70.
[9] R.I. Fromont, Mater. Process. Rep. 7 (2) (1992) 2–8.
[10] D.C. Dunand, J.L. Sommer, A. Mortensen, Metall. Trans. A 24A (1993) 2161–2169.
[11] D.C. Dunand, Mater. Manuf. Process. 10 (1995) 373–382.
[12] H. Nakae, H. Fujii, K. Nakajima, A. Goto, Mater. Sci. Eng. A223 (1997) 21–28.
[13] S. San Marchi, A. Mortensen, Metall. Mater. Trans. A 29A (1998) 2819–2827.
[14] Y. Chen, D.D.L. Chung, J. Mater. Sci. 31 (1996) 2117–2125.
[15] Y. Um, R. Watanabe, J. Jpn. Inst. Met. 58 (1994) 559–568.
[16] K. Suganuma, Mater. Lett. 16 (1993) 22–34.
[17] H. Chen, M. Kaya, R.W. Smith, Materials 13 (1992) 180–193.
[18] D.L. Joslin, D.S. Easton, C.T. Liu, S.A. David, Mater. Sci. Eng. A 192–193 (1995) 544–548.
[19] D.L. Joslin, D.S. Easton, C.T. Liu, S.S. Babu, S.A. David, Intermetallics 3 (1995) 467–481.
[20] L.Z. Zhuang, L. Buekenhout, J. Duszczyk, Scripta Metall. Mater. 30 (1994) 909–914.
[21] S. Stecura, Thin Solid Films 150 (1987) 15–40.
[22] P.P. Bandyopadhyay, PhD Thesis, IIT Kharagpur, India, 2000.

[23] C.T. Sims, N.S. Stoloff, W.C. Hagel, Superalloys II, Wiley Interscience, New York, 1987.
[24] P. Kofstad, High Temperature Corrosion, Elsevier Applied Science, New York, 1988.
[25] C. Wagner, Z. Elektrochem. 63 (1959) 772–779.
[26] F. Gesmundo, Y. Niu, B. Pieraggi, F. Viani, Oxid. Met. 49 (1998) 115–122.
[27] Y.S. Li, Y. Niu, F. Gesmundo, F.H. Wang, Corros. Sci. 44 (2002) 1457–1468.